PNAS RESEARCH ARTICLE | NEUROSCIENCE

Broken time-reversal symmetry in visual motion detection

Nathan Wu[a,1], Baohua Zhou[b,1], Margarida Agrochao[b], and Damon A. Clark[b,c,d,e,f,2]

Edited by William Bialek, Princeton University, Princeton, NJ; received May 30, 2024; accepted January 9, 2025

Our intuition suggests that when a movie is played in reverse, our perception of motion at each location in the reversed movie will be perfectly inverted compared to the original. This intuition is also reflected in classical theoretical and practical models of motion estimation, in which velocity flow fields invert when inputs are reversed in time. However, here we report that this symmetry of motion perception upon time reversal is broken in real visual systems. We designed a set of visual stimuli to investigate time reversal symmetry breaking in the fruit fly *Drosophila*'s well-studied optomotor rotation behavior. We identified a suite of stimuli with a wide variety of properties that can uncover broken time reversal symmetry in fly behavioral responses. We then trained neural network models to predict the velocity of scenes with both natural and artificial contrast distributions. Training with naturalistic contrast distributions yielded models that broke time reversal symmetry, even when the training data themselves were time reversal symmetric. We show analytically and numerically that the breaking of time reversal symmetry in the model responses can arise from contrast asymmetry in the training data, but can also arise from other features of the contrast distribution. Furthermore, shallower neural network models can exhibit stronger symmetry breaking than deeper ones, suggesting that less flexible neural networks may be more prone to time reversal symmetry breaking. Overall, these results reveal a surprising feature of biological motion detectors and suggest that it could arise from constrained optimization in natural environments.

motion detection | symmetry | symmetry breaking | algorithm | *Drosophila*

Significance

In neural circuits, symmetries in processing can tell us about the computations being performed and can echo symmetries in the inputs to the circuit. For example, because all local motion signals in a movie reverse direction when the movie is reversed in time, intuition suggests that motion percepts in response to the time-reversed movie should exactly reverse, too. Surprisingly, with some stimuli, this perceptual reversal does not occur, revealing a broken time reversal symmetry. This research identifies conditions for breaking time reversal symmetry in animal motion percepts as well as in analytical and computational models for motion estimation. The results show how this intuitive symmetry can be broken in systems optimized to perform with naturalistic inputs.

Imagine a movie of a hiker crossing a stream (Fig. 1*A*). The hiker walks into frame from the left, travels across a footbridge, and continues out of frame on the right. Now, imagine the same video, but played in reverse. The hiker backpedals from right to left. The hiker, originally moving rightward, has reversed direction and is now moving leftward. Intuitively, when we reverse time, we expect that our motion percepts should reverse as well (Fig. 1*B*). It is not just our intuition: If we define velocity as displacement over time, playing the movie backward in fact results in equal and opposite velocities at each location in the movie (Fig. 1*C*). Thus, a time-forward and time-reversed movie are likely to be visually distinguishable from one another (as with the hiker crossing a bridge), but the local velocities in the two movies are exactly opposite. Consequently, one might expect that motion percepts in response to a time-reversed movie should be perfectly opposite to the time-forward movie.

Indeed, classical models for biological motion estimation produce exactly inverted responses upon time reversal, matching both our intuition and the reversal of the true local velocities. Because local velocities are a latent quality of the visual scene, they must be inferred or estimated using a nonlinear operator (2, 3). The Hassenstein-Reichardt correlator model and the motion energy model, for instance, both estimate the direction and speed of visual motion by computing and averaging pairwise correlations in light intensity over space and time (3, 4). When a stimulus is played in reverse to these models, their output is exactly inverted from when that stimulus is played forward in time. Other models that are optimized to estimate visual motion have similar properties. In particular, a Bayesian model for motion estimation (5) gives a limiting solution that detects gradients and reverses under stimulus time reversal. One of the most widespread machine-vision techniques for estimating visual motion (6) estimates local velocities with a method that gives an opposite result when inputs are reversed in time. (These results are shown in *SI Appendix*, Appendix 1) Thus, a formidable suite of visual motion estimation models, in addition to our intuition, obey what we call response time reversal symmetry, since reversing time in any stimulus reverses the response, as measured by the model output. However, as we will explore in this research, estimators need not possess the same symmetries as the latent quantities they estimate, so that even though velocities invert under time reversal, a motion estimator is not required to.

Studying symmetries and when they are broken has led to deeper understanding in both physics and biology. In physics, symmetries and invariances play an outsized role

Author affiliations: [a]Yale College, New Haven, CT 06511; [b]Department of Molecular Cellular and Developmental Biology, Yale University, New Haven, CT 06511; [c]Department of Physics, Yale University, New Haven, CT 06511; [d]Department of Neuroscience, Yale University, New Haven, CT 06511; [e]Quantitative Biology Institute, Yale University, New Haven, CT 06511; and [f]Wu Tsai Institute, Yale University, New Haven, CT 06511

Author contributions: N.W., B.Z., and D.A.C. designed research; N.W., B.Z., and M.A. performed research; N.W., B.Z., and D.A.C. analyzed data; and N.W., B.Z., and D.A.C. wrote the paper.

The authors declare no competing interest.

This article is a PNAS Direct Submission.

Copyright © 2025 the Author(s). Published by PNAS. This article is distributed under Creative Commons Attribution-NonCommercial-NoDerivatives License 4.0 (CC BY-NC-ND).

[1]N.W. and B.Z. contributed equally to this work.

[2]To whom correspondence may be addressed. Email: damon.clark@yale.edu.

This article contains supporting information online at https://www.pnas.org/lookup/suppl/doi:10.1073/pnas.2410768122/-/DCSupplemental.

Published March 6, 2025.

Downloaded from https://www.pnas.org by Nathan Wu on May 13, 2025 from IP address 178.238.172.182.

in understanding the equations that govern physical phenomena (7, 8). In neuroscience, interesting neural processing properties are often the result of maintaining or breaking symmetries. In visual processing in particular, symmetries and asymmetries of the natural world end up reflected in neural computations. For instance, the translation invariance of visual scenes across the visual field is reflected in the tiling of feature detectors in vertebrates and invertebrates across visual space (9). In orientation detectors in the mammalian cortex, rotational symmetry is broken, so that there are more cells aligned with vertical and horizontal orientations, in agreement with natural scene statistics (10). Also, in the mammalian cortex, space reversal symmetry, or left–right symmetry, is broken during retinal development to favor front-to-back visual motion that coincides with optic flow due to forward movement (11). Light–dark symmetry is broken in natural scenes, and this is reflected in the number of ON and OFF channels in the retina (12) as well as in algorithms for motion estimation in flies and vertebrates (13, 14). Moreover, in artificial neural networks, symmetries of the data and the network play critical roles in understanding how machine learning architectures work (15).

To our knowledge, the time reversal symmetry we have outlined has not been previously investigated in neural circuit computations. This sort of time reversal symmetry relates to the algorithms employed by the circuits, and is distinct from ideas of reversibility and entropy in thermodynamics, which have previously been examined in neural populations and fMRI (16–19). By investigating time reversal symmetry in the computation of visual motion, our goal is to identify and understand the conditions under which a motion percept does or does not exactly reverse when a particular stimulus is reversed in time. This understanding will help reveal the structure of the algorithms underlying biological motion estimators and suggest how this broken symmetry arises in visual circuits that may be optimized to estimate motion (20).

Here, we report that motion percepts in the fruit fly *Drosophila* break time reversal symmetry with specific visual stimuli, in contrast both to classical models for motion estimation and to our intuition about time reversal. In this study, we first evaluated time reversal symmetry breaking in responses to previously used visual stimuli. We then developed methods to investigate the properties of stimuli that induce motion percepts that break time reversal symmetry. Using these methods, we identified a host of stimuli that reveal time reversal symmetry breaking in fly motion estimation. To better understand this symmetry breaking, we optimized a suite of simple motion estimation models to investigate what properties of those estimators and their training data result in breaking time reversal symmetry in response to particular stimuli. We also derived analytically necessary conditions for time reversal symmetry breaking in motion estimators. Overall, algorithms optimized to estimate motion in scenes with non-Gaussian contrasts showed time reversal symmetry breaking, as in flies, while those trained using Gaussian contrasts showed no or much less time reversal symmetry breaking. This was surprising because all the training data maintained time reversal symmetry, indicating that the time reversal symmetry was broken by contrast statistics during optimization. These results show how optimization can result in unintuitive regimes of symmetry breaking in neural systems and explain why motion percepts do not always reverse when stimuli are played backward.

Results

Certain Stimuli Elicit Behavioral Responses That Break Time Reversal Symmetry. A variety of visual stimuli break response time reversal symmetry in animal motion percepts (Fig. 1). These motion percepts are the product of the animal's visual motion estimation algorithm and can be measured through behavioral responses. To examine directional percepts in *Drosophila*, we tethered flies above an air-suspended ball, surrounded by a panoramic display (Fig. 1*D*) (21). This behavioral assay takes advantage of the optomotor turning response, in which flies and other insects turn in the direction of perceived motion presented

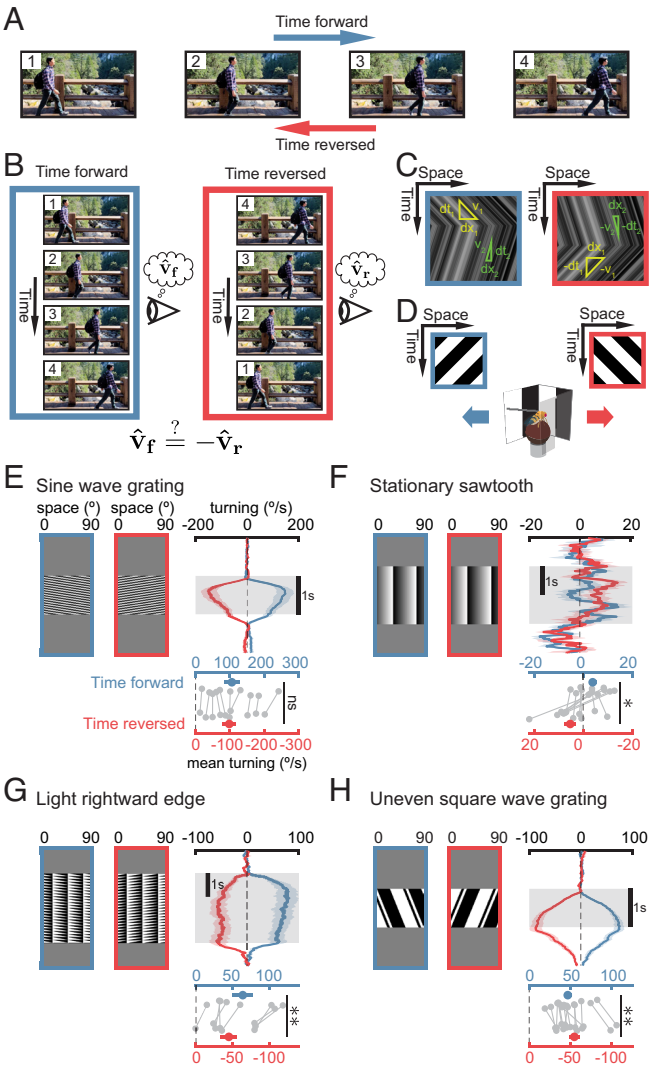

Fig. 1. Fly behavioral responses to some stimuli break time reversal symmetry. $*P < 0.05$, $**P < 0.01$ by the Student *t* test with paired samples. (*A*) A movie of a hiker walking forward and rightward becomes a hiker walking backward and leftward when played in reverse. (*B*) Intuitively, the motion of all objects in a movie reverses upon time reversal. Time reversal symmetry of the motion percept is broken when perceived motion vectors are not equal and opposite. (*C*) Under time reversal, the magnitude and direction of all local velocities in a movie are equal and opposite to those when the movie is reversed in time. (*D*) Motion perception in *Drosophila* was measured with optomotor turning. Tethered flies were placed above air-supported balls while time forward and time-reversed stimuli were projected onto panoramic displays. Fly turning was measured by rotation of the ball. (*E*) Responses to drifting sine wave gratings played time forward and time reversed (*Left*). Time traces of mean and SEM fly response to each (*Top Right*). Time traces were averaged to obtain the mean response during the stimulus presentation (*Bottom*). Time reversal symmetry breaking is tested by whether the response to the forward stimulus is significantly different from the opposite of the response to the reversed stimulus. Gray points represent individual fly responses to each stimulus, with lines connecting responses from the same fly. N = 9 flies. (*F*) As in (*E*), but for a stationary contrast sawtooth (1), which is time reversal symmetric. N = 8 flies. (*G*) As in (*E*), but for local light edges tessellated across space and time. N = 8 flies. (*H*) As in (*E*), but for square wave grating with bars of unequal widths. N = 8 flies.

Downloaded from https://www.pnas.org by Nathan Wu on May 13, 2025 from IP address 178.238.172.182.

across the visual field (4). Some commonly used stimuli, like drifting sinusoidal contrast gratings, do result in behaviors that obey time reversal symmetry (Fig. 1*E*). That is, when the drifting grating is played in reverse, the turning response exactly reverses, in line with intuition as well as classical motion estimation models, including the Hassenstein-Reichardt correlator (4) and the Lucas–Kanade method (6) (*SI Appendix*, Appendix 1).

One simple stimulus that elicits percepts that break time reversal symmetry is a stationary sawtooth in contrast (Fig. 1*F*), which elicits motion percepts in humans (22), primates (23), cats (24), fish (25), and flies (1). (This sawtooth stimulus and a different version of this stimulus, designed to create strong illusory motion percept in humans (26), are shown in *SI Appendix*, Fig. S1.) Since this stimulus is stationary, it is identical when played forward or backward. Consequently, forward and backward presentations of the stimulus must result in identical perceptual responses. Time reversal symmetry of perceptual responses is obeyed when responses invert under time reversal, since all velocities in a stimulus invert under time reversal. Therefore, the only possible response to the stationary sawtooth stimulus that obeys time reversal symmetry is zero. Any net turning response to this stimulus breaks time reversal. Indeed, flies turn in response to this stationary stimulus (Fig. 1*F*), and prior work has shown that this response requires visual neurons that detect motion (1). Flies also respond to nonstationary versions of this stimulus in ways that break time reversal symmetry (*SI Appendix*, Fig. S2).

Other stimuli with strong local motion signals can also elicit behaviors that break time reversal symmetry. For instance, a stimulus consisting of local light edges elicits turning with opposite sign when it is reversed in time, but the turning strengths are not equal (Fig. 1*G*), so the response to this also breaks time reversal symmetry. Because time-reversed light edges are equivalent to dark edges moving in the opposite direction, this result corroborates previous findings that light and dark edge motion estimation are imbalanced in fruit flies (1, 13, 27–29). The response symmetry breaking can also be uncovered by a rigidly translating pattern: A periodic square wave grating with light and dark bars of unequal widths can elicit responses that are not time reversal symmetric (Fig. 1*H*). This drifting stimulus, similarly to the local light edge stimulus, elicits opposite but unequal turning upon time reversal. Last, stimuli that are the identical when played forward or backward can be constructed with oppositely oriented light and dark edges (27). These stimuli elicit behavior that breaks time reversal symmetry because they induce nonzero turning responses which remain unchanged upon time reversal (rather than inverting) (*SI Appendix*, Fig. S2), similar to the stationary sawtooth stimulus. The fly's turning behavior to these stimuli is the result of its motion estimation algorithm. While some stimuli result in responses that are time reversal symmetric (for instance, those in Fig. 1*E*), the algorithm's broken time reversal symmetry can be revealed by a diverse set of stimuli.

Examining the Full Suite of Stimulus Symmetries. Some stimuli can reveal an algorithm's time reversal symmetry breaking, but it is not clear what properties they have in common. To look for commonalities, we began by examining whether the symmetries possessed by individual stimuli contribute to whether they reveal symmetry breaking in percepts. We focused on time reversal, space reversal, and contrast reversal symmetries of the stimuli. Time reversal plays the stimulus backward; space reversal flips the position axis of the stimulus; contrast reversal inverts the contrast of all pixels, with light pixels turning dark and dark pixels turning light. A stimulus possesses a specific symmetry if the transformed stimulus is identical to the original, allowing for a shift in space or time (Fig. 2*A*). For instance, a drifting sinusoidal grating (Figs. 1 *E* and 2 *A*) possesses a contrast reversal symmetry because when contrast is reversed, the resulting stimulus is identical to the original up to a phase shift.

There are three distinct classes of symmetries we will deal with in the coming analyses. First, we have symmetries of the function S that represents the stimulus. Second, we have symmetries of the velocity: The true velocity field in any stimulus reverses when the stimulus is played in reverse. Last, we have symmetries of the velocity estimator, which need not match the symmetries of the velocity it is estimating. Our goal is to identify the circumstances in which the neuronal velocity estimator (reflected in the fly's behavior) does not match the symmetry of the velocity.

To concisely describe symmetries and transformations of the stimuli, we represent the time reversal operator as Θ, the contrast reversal operator as Γ, and the space reversal operator as χ (see *SI Appendix*, Methods for definitions). For instance, the contrast reversed version of stimulus S is notated as $\Gamma[S]$. Once an operator is applied to a stimulus S, we represent the altered stimulus with a left subscript: In other words, $\Gamma[S] = {}_{\Gamma}S$. In this notation, the stimulus S is said to be contrast, time, and space reversal symmetric if ${}_{\Gamma}S = S$, ${}_{\Theta}S = S$, and ${}_{\chi}S = S$, respectively. Time reversal, contrast reversal, and space reversal are commutative and consequently can be noted as sequential left subscripts: For instance, $\Theta[\Gamma[S]] = \Gamma[\Theta[S]] = {}_{\Gamma\Theta}S = {}_{\Theta\Gamma}S$. The response, $R[S]$, represents the integrated turning response of flies to the stimulus S. The drifting sinusoid possesses contrast symmetry (Γ symmetry), space-time symmetry ($\chi\Theta$ symmetry), and contrast-space-time symmetry ($\Gamma\chi\Theta$ symmetry) (Fig. 2*A*).

We cataloged the symmetries in the initial stimuli we examined (Fig. 1 and *SI Appendix*, Fig. S2) and found that these stimuli covered a relatively small fraction of all possible symmetry combinations (Fig. 3, *Top*). Some symmetries, especially space-contrast (${}_{\chi\Gamma}S = S$), appeared overrepresented among those that resulted in behavior that broke time reversal symmetry.

To examine how stimulus symmetries might reveal symmetries of the velocity estimator, we set out to design a suite of stimuli that could fill in all possible combinations of symmetries in Fig. 3. To do that, we established a method to design edge-tile stimuli (*SI Appendix*, Methods). These stimuli use edge-tiles that contain either light or dark edges, moving either to the right or to the left (Fig. 2*B*). After arranging groups of 8 individual edge-tiles into rectangular unit cells, we could tessellate the unit cells in space and time (Fig. 2 *C* and *D*). Since there are 4 possible edge-tiles at each location in the unit cell, there are $4^8 = 65,536$ possible unit cells, or patterns, though not all result in unique stimuli after tessellation. To check for different symmetries in stimuli made with each pattern, we compared the stimulus transformed with the symmetry operators to the original stimulus at all possible phase shifts (for most patterns, 4 in space, 2 in time; see *SI Appendix*, Methods). If the transformed and original stimuli contain the identical unit cell at some phase offset, then the stimulus possesses that symmetry. For each unit cell, we enumerated whether it has a space reversal symmetry, time reversal symmetry, contrast reversal symmetry, or various combinations of these (Fig. 2 *C* and *D*).

Next, we selected 24 different edge-tile stimulus patterns to test on flies. For each possible combination of symmetries, we chose two patterns (Fig. 3, *Bottom*). Four patterns were chosen with no symmetries. Where possible, the specific patterns were selected to minimize contrast discontinuities in time, for instance a dark region that instantaneously becomes light. Also where possible,

Downloaded from https://www.pnas.org by Nathan Wu on May 13, 2025 from IP address 178.238.172.182.

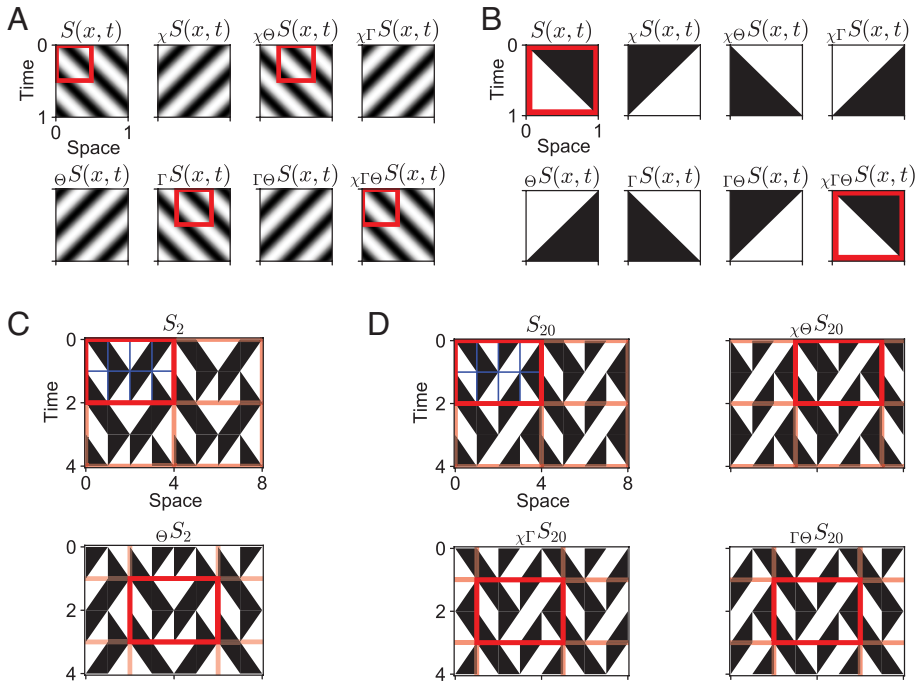

Fig. 2. Edge-tile stimuli can be created with different combinations of spatial, temporal, and contrast symmetries. (*A*) All stimuli can be transformed through space reversal, time reversal, or contrast reversal, denoted with operators χ, Θ, and Γ. A stimulus S is O symmetric if $O[S(x,t)] = {}_{O}S(x,t)$ is the same as $S(x,t)$, allowing for shifts in space and time. A drifting sinusoid grating, shown here, is contrast (Γ) symmetric, space-time ($\chi\Theta$) symmetric, and contrast-space-time ($\Gamma\chi\Theta$) symmetric because the corresponding transformations return the same stimulus tessellated in space and time (boxed in red). (*B*) Edge-tiles consist of single light or dark edges, moving *Left* or *Right*. A light, rightward edge-tile can be transformed into any other single edge-tyle type (light/dark, rightward/leftward) through space reversal, time reversal, or contrast reversal. Each single edge-tile is $\chi\Gamma\Theta$ symmetric. (*C*) Stimuli with different combinations of symmetries can be created by placing arrays of individual edge-tiles into unit cells. S_2 is composed of a unit cell of 8 edges-tiles in a 4 by 2 grid (outlined in red), which is tessellated over space and time. S_2 is time reversal symmetric because reversing the entire stimulus in time results in a stimulus in which the same unit cell can be found (phase shifted in time and space from its original location and time). See *SI Appendix*, Methods for details on creating these stimuli; see Movie S1 for a visualization of the stimuli. (*D*) Stimuli can possess multiple combinations of symmetries. S_{20} has a unit cell that is 4 by 2 and is $\chi\Theta$, $\chi\Gamma$, and $\Gamma\Theta$ symmetric, meaning that performing each of those pairs of reversals results in a stimulus possessing the same 4 by 2 unit cell, outlined in red.

stimuli for each combination of symmetries were selected to cover cases where stimuli had both nonzero and zero net motion when averaged over time and space.

Fly Responses to Certain Edge-Tile Patterns Break Time Reversal Symmetry. We presented each of the chosen edge-tile patterns to wildtype *Drosophila melanogaster* flies. Since the patterns have only one spatial dimension, we presented them on screens by replicating the same pattern on all pixel rows vertically (Movie S1). Flies responded to many of these stimuli, turning on average more in one direction than in the other (Fig. 4 *A* and *B*). As we did before, we averaged the turning responses over time and over trials to obtain a single mean response to each stimulus for each fly (*SI Appendix*, Fig. S3). We began by examining responses to two example stimuli, S_2 and S_{20}, which elicited responses that broke time reversal symmetry (Fig. 4 *A* and *B*). We plotted responses to different presentations of the stimuli (Fig. 4 *i* and *ii*).

To analyze symmetry breaking in these responses, we defined three metrics to identify time, contrast, and contrast-time reversal symmetry breaking (Fig. 4 *iii*). These metrics are based on the symmetries of the veridical velocity in a scene: The velocity reverses under time reversal, reverses under space reversal, and remains the same under contrast reversal (Fig. 1 *C*). The velocity estimator, which extracts latent velocity signals from the stimulus, need not obey the same symmetries as the velocity it estimates. For instance, a Bayes optimal velocity estimator may not respond the same way to a stimulus when it is contrast reversed (14). We will define broken symmetries in the velocity estimator as deviations from the symmetries of the velocity field. First, the time reversal symmetry metric: A response breaks time reversal symmetry if the response to the stimulus played forward plus the response to it played backward is different from zero, that is, when the metric, $R[S] + R[_{\Theta}S]$, is different from 0. This formulation is the same definition used in our earlier analysis (Fig. 1). Second, since velocity does not change under contrast reversal, a response breaks contrast reversal symmetry if the response to the stimulus minus the response to the contrast reversed stimulus is different from zero, that is, when the metric $R[S] - R[_{\Gamma}S] \neq 0$. Breaking contrast-time reversal happens when the response to the stimulus plus the response to its contrast and time-reversed variant is different from zero, that is, when the metric $R[S] + R[_{\Gamma\Theta}S] \neq 0$. When these metrics were statistically significantly different from zero, we judged the response symmetry broken for that stimulus (Fig. 4 *iii*). We did not test for space reversal symmetry: When mounting flies, we expect some mild left–right asymmetries in how they are mounted, which we do not want to mistake for true biological asymmetries. Thus, we compute fly responses as half of their turning to the stimulus presented clockwise minus half their turning when it is presented counterclockwise (*SI Appendix*, Methods). This eliminates potential experimental asymmetry and also prevents us from measuring space reversal symmetry breaking in the response.

Summarizing Responses to Stimuli with Different Symmetries. To better understand how specific symmetries in the stimuli influenced responses, we first sorted the stimuli in order of the strength of the response's time reversal and contrast-time reversal symmetry metrics (Fig. 5 *A* and *B* and *SI Appendix*, Fig. S4 *A* and *B*). To do this, we plotted the signed symmetry metrics for each stimulus: $R[S] + R[_{\Theta}S]$ and $R[S] + R[_{\Gamma\Theta}S]$. Given asymmetries

Downloaded from https://www.pnas.org by Nathan Wu on May 13, 2025 from IP address 178.238.172.182.

Symmetry							
Θ	Γ	$\Gamma\Theta$	$\chi\Theta$	$\chi\Gamma$	$\chi\Gamma\Theta$	Stimuli	XT plots (Time, Space)
					●	light edge, uneven square wave grating	
	●		●		●	sine wave grating	
●				●	●	stationary sawtooth	
●						S_1, S_2	
	●					S_3, S_4	
		●				S_5, S_6	
			●			S_7, S_8	
				●		S_9, S_{10}	
					●	S_{11}, S_{12}	
●	●	●				S_{13}, S_{14}	
	●		●		●	S_{15}, S_{16}	
●				●	●	S_{17}, S_{18}	
		●	●	●		S_{19}, S_{20}	
						S_{21}, S_{22}, S_{23}, S_{24}	

Fig. 3. Table of symmetries in stimuli in Fig. 1. The upper part of the table enumerates symmetries in our stimuli from Fig. 1, while the lower part enumerates those in the edge-tile stimuli. A dot in the column means that the stimulus possesses that symmetry. See *SI Appendix*, Methods for the definition of the symmetries with periodic stimuli. The different symmetries are Θ (time reversal), Γ (contrast reversal), χ (space reversal), $\Gamma\Theta$ (contrast-time reversal), $\chi\Theta$ (space-time reversal), $\chi\Gamma$ (space-contrast reversal), and $\chi\Gamma\Theta$ (space-contrast-time reversal).

in the fly's turning to light and dark edges (Fig. 1) (13, 27–30), one might hypothesize that the turning to our edge-tile patterns could be predicted just by examining the number of light and dark edges. However, we did not observe any obvious patterns in the strength of the symmetry breaking as a function of the net number of light and dark edges in the stimuli.

To more quantitatively assess the relationship between the time reversal symmetry metric and the count of light and dark edges in the stimuli, we fit linear models to predict the metric by weighting the net light and dark edge count in the edge-tile stimuli. The linear models accounted for 24 and 0.1% of the variance in the time reversal symmetry and contrast-time reversal symmetry metrics. Significant positive weighting was placed on the net dark edges in the case of time reversal symmetry (Fig. 5*C*). No significant weighting was placed on net light or dark edges in the case of contrast-time reversal symmetry (Fig. 5*E*). No constant bias term was fit in the model, as we expect rightward edges of a given polarity to yield the exact opposite percept as leftward edges of the same polarity. Notably, the stimulus S_{14} had net 0 light and dark edges but fly responses showed strong symmetry breaking with stimulus time reversal. The six strongest responses breaking contrast-time symmetry all also had net zero light and dark edges (Fig. 5, and *SI Appendix*, Fig. S4*B*). Similarly, many stimuli that broke contrast reversal symmetry in responses also had no net light or dark edges (*SI Appendix*, Fig. S4). Because light and dark edge counts do not predict time reversal symmetry breaking of behavioral responses, the phenomenon is not simply a result of differing strengths of responses to light and dark edges (see also *SI Appendix*, Fig. S2 for a nonpredictive example).

We next examined how different stimulus symmetries impacted the strength of response symmetry breaking. Since the symmetries in a stimulus have no direction, we flipped all the measured metrics to have a positive mean response (Fig. 5 *D* and *F* and *SI Appendix*, Fig. S4 *D* and *E*). We could then ask how the stimulus symmetries affected the amplitude of the symmetry metrics for both time reversal and contrast-time reversal symmetries. Again, we did not see an obvious pattern in the stimulus symmetries that elicited the strongest response symmetry breaking. We therefore fit linear models to predict the strength of the symmetry breaking from the suite of stimulus symmetries. These models predicted 25 and 50% of the variance in the time reversal and contrast-time reversal behavioral symmetry breaking. The most significant weight was a negative weighting on time-space-contrast symmetry for the response time reversal symmetry breaking (Fig. 5*D*) and a positive weighting on contrast-time symmetry for the response contrast-time reversal symmetry breaking (Fig. 5*F*). This second case shows that flies exhibited net turning to stimuli that were identical when transformed by reversing both time and contrast. This is conceptually similar to flies turning to stimuli that are identical under time reversal (Fig. 1 and *SI Appendix*, Fig. S2). Overall, stimulus symmetries showed some correlations but did not yield definitive contributions of specific properties to revealing broken time reversal symmetry in fly behavior.

Optimized Neural Networks Predict Stimulus Velocity. Stimulus symmetries did not provide definitive answers about what stimulus features produce responses that break time reversal symmetry, so we opted to take a parallel approach. In this approach, instead of focusing on stimulus properties directly, we worked to understand what factors cause certain motion estimators to break time reversal symmetry. Biological motion estimators have evolved under natural selection, and we wondered how that process of optimization could influence time reversal symmetry breaking in responses. We thus set out to construct neural network models and train them to predict the velocity of a scene. Our goal was not to exactly reproduce the fly's visual responses, but rather to understand what features of the neural network and training regime result in breaking the response's time reversal symmetry.

We began by creating a set of synthetic motion stimuli by rigidly translating panoramic images from a database of natural scenes (31) (Fig. 6*A*). For simplicity, we considered only motion in the horizontal direction, mimicking the fly's rotation in the yaw dimension that we measured in our earlier experiments. Velocity trajectories were drawn from a Gaussian distribution with a correlation half-decay time of 200 ms (Fig. 6*B*). Critically, this dataset is statistically identical when played forward or backward in time, so any time reversal symmetry breaking observed in model responses cannot be the result of broken time reversal symmetry in the training data. For each data sample with a certain velocity trace (Fig. 6*B*), we created a counterpart with spatial coordinates reversed horizontally so that the training dataset had perfect left–right symmetry (Fig. 6*C*). We then trained convolutional neural network models on this motion dataset, so that the models predicted the instantaneous scene velocity based on recent observations of the

Downloaded from https://www.pnas.org by Nathan Wu on May 13, 2025 from IP address 178.238.172.182.

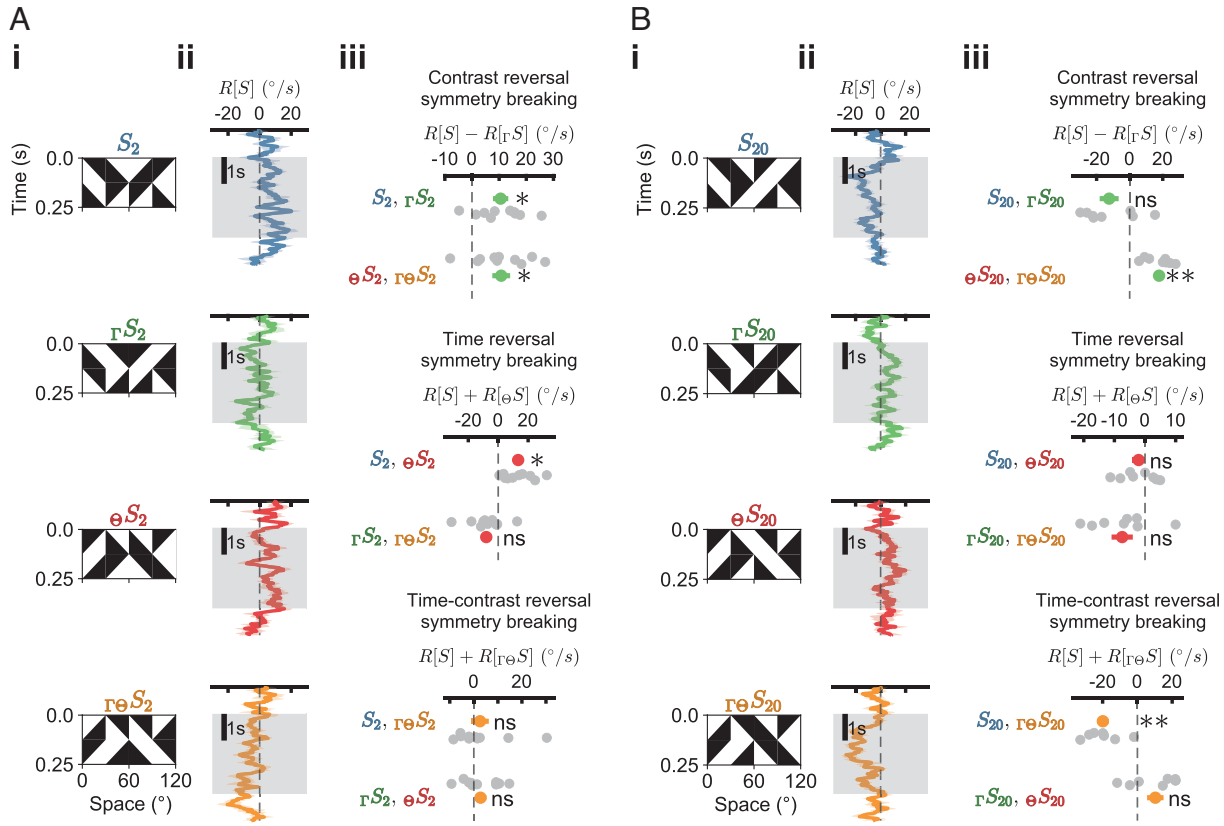

Fig. 4. Fly responses to edge-tile stimuli can break time reversal symmetry. Edge-tile stimuli were presented for a total of three seconds, with each individual edge moving at 240°/s. N = 8 to 10 flies for each trace. *P < 0.05, **P < 0.01 by the Student t test, with Holm–Bonferroni correction for the 6 comparisons for each stimulus. (*A*) Fly responses to the stimulus S_2, which is itself Θ symmetric but generates responses that break time reversal symmetry. (*i*) The stimulus and its reversals in time, contrast, and contrast-time. (*ii*) Time traces of mean fly responses to these four transformations of the stimuli. (*iii*) Contrast symmetry breaking is measured by subtracting the time averaged responses to the original stimulus and the contrast reversed stimulus (green, *Top*). Time and contrast-time symmetry breaking is measured by summing time-averaged responses to the original and time-reversed or contrast-time-reversed stimuli, respectively (red and orange, *Bottom*). Gray points represent subtracted/summed responses from individual flies. Symmetry breaking occurs when these subtracted/summed responses are significantly different from 0, as indicated by the asterisks. (*B*) As in (*A*), but for the stimulus, S_{20}, which is $\chi\Theta$, $\chi\Gamma$, and $\Gamma\Theta$ symmetric.

stimulus contrast over time (Fig. 6*C*). We began with a simple model, which also resembles the motion detectors in the fly eye. This model had two channels that each received inputs from three adjacent points in space, resembling the ON and OFF motion detectors in the fly's eye (28, 32). This model is similar to prior models used in simulations (33) and task optimization (34). The training converged after ~300 epochs (*SI Appendix*, Fig. S5) and typical trained models predicted ~90% of the variance in scene velocity of a hold-out test dataset (*SI Appendix*, Fig. S5). Since these models have no unique optimized solution, we trained 500 models, each with different initializations, to generate a rich group of trained motion estimators to analyze.

Optimized Model Responses Break Time Reversal Symmetry. To investigate time reversal symmetry in the responses of these trained models, we tested them on three synthetic stimuli that had resulted in time reversal symmetry breaking in fly behavior (Fig. 6 *D*–*F*): 1) moving light edges and their time-reversed counterparts; 2) stationary sawtooth contrast stimuli; and 3) the stimulus S_{14}, which elicited strong turning responses and possesses time, contrast, and contrast-time reversal symmetry.

The trained models responded more strongly to light edges than to time-reversed light edges (dark edges), indicating that they had broken time reversal symmetry in their responses (Fig. 6*G*). The degree of symmetry breaking here was measured by the time reversal symmetry metric for the model's response, $R_M[S] + R_M[_\Theta S]$, where R_M is the model's response. This metric would be zero for a response showing time reversal symmetry and nonzero otherwise.

When presented with a stationary sawtooth stimulus or with the stimulus S_{14}, a model with perfect time reversal symmetry will generate a response of zero, while a model that breaks time reversal symmetry will have a nonzero response. When our trained models were presented with sawtooth stimuli or S_{14}, they had nonzero responses and time reversal symmetry metrics (Fig. 6 *H* and *I*), indicating the responses broke time reversal symmetry.

For all three stimuli, these trained models broke time reversal symmetry in the same direction as the fly data (Figs. 1 and 5): the model's time reversal symmetry metrics, $R_M[S] + R_M[_\Theta S]$, were the same sign as the fly's metrics, $R[S] + R[_\Theta S]$ (Fig. 1). However, this agreement should not be viewed as significant, since it depends on the stimulus parameters used, such as contrast levels (*SI Appendix*, Fig. S5). Rather, the important result is that these trained models broke time reversal symmetry.

Time Reversal Symmetry Breaking Depends on the Contrast Distribution in the Training Data. We wanted to understand which properties of the models and the training data led to breaking time reversal symmetry in the responses. We therefore created synthetic image datasets with contrast distributions different from the natural scenes we used earlier (Fig. 7*A*). In natural scenes, the distribution of the pixel contrast values is right-skewed and highly kurtotic (Fig. 7*A*) (35). This skew has been proposed to explain a suite of fly directional behavioral responses (36). We therefore decided to manipulate the pixel distribution in the training data to see how it affects response time reversal symmetry breaking. To do this, we created three synthetic training datasets (Fig. 7*A*). The first one

Downloaded from https://www.pnas.org by Nathan Wu on May 13, 2025 from IP address 178.238.172.182.

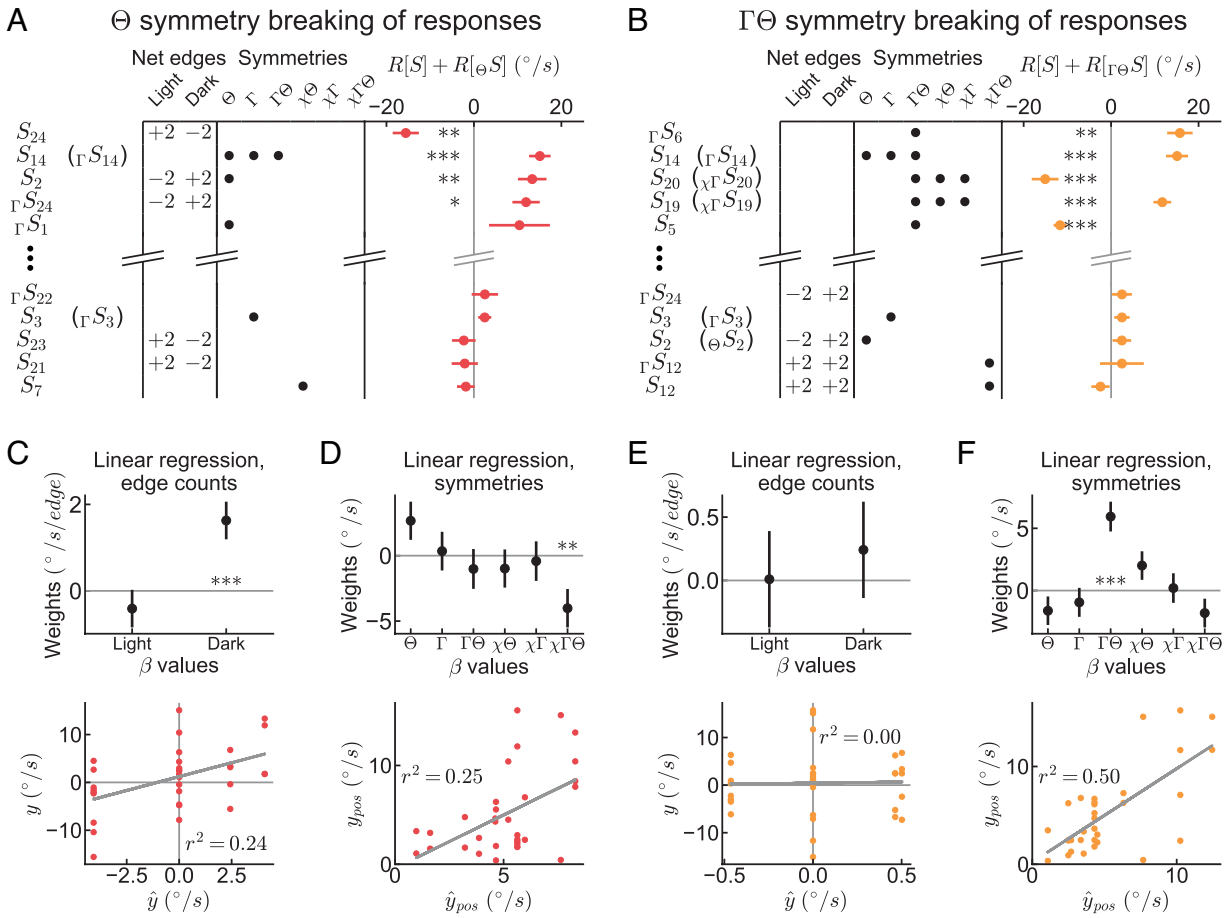

Fig. 5. Many stimuli elicit behavior that breaks time reversal symmetry, but stimulus symmetries only modestly predict degree of time reversal symmetry breaking. (*A*) Time reversal symmetry breaking in response to edge-tile stimuli. Net edge counts, symmetries, and time reversal symmetry breaking of responses for selected stimuli. The 5 stimuli that induce the greatest degree of symmetry breaking and the 5 stimuli that induce the least symmetry breaking are shown. Stimuli in parentheses indicate that the stimulus being tested possesses a symmetry (or multiple symmetries) that permit combining response asymmetry metrics from both S and $_\Gamma S$ into a single measurement. N = 8 to 11 flies for each measurement. For the data, error bars are 1 SEM; $^*P < 0.05$, $^{**}P < 0.01$, $^{***}P < 0.001$ by the Student t test, with Holm–Bonferroni correction for 6 comparisons for each stimulus. (*B*) As in (*A*), but for contrast-time reversal symmetry breaking in responses. (*C*) A linear model with no bias term was fit to predict the symmetry breaking metric of the response from the net light and dark edge counts. The model can be expressed as $\hat{y} = \beta_{light} \cdot C_{light} + \beta_{dark} \cdot C_{dark}$, where C_{light} and C_{dark} represent counts of net light and dark edges, respectively, and β_{light} and β_{dark} represent the fitted weights. The values of β are shown in the top graph, and a regression between the predicted and actual responses is shown below. The variance accounted for by the model is noted by the r^2 value. For the linear fits, error bars are 1 SEM; $^*P < 0.05$, $^{**}P < 0.01$ $^{***}P < 0.001$ by standard CI estimation. (*D*) A linear model with a bias term was fit to predict the strength of the symmetry breaking metric of the response from the symmetries present in the stimulus. The strength of the symmetry breaking metric was computed by making all responses positive by flipping all negative average responses. The model can be expressed as $\hat{y}_{pos} = b + \sum_{i \in \{\Theta, \cdots, \chi\Gamma\Theta\}} \beta_i \cdot B_i$, where B_i represents a binary variable indicating whether or not a stimulus possesses the i symmetry and β_i represents a corresponding fitted weight. Fitted weights and regression are as in (*C*). (*E*) As in (*C*), but for contrast-time reversal symmetry breaking. (*F*) As in (*D*), but for contrast-time reversal symmetry breaking.

simply reversed the sign of the pixel contrast values of the natural scene training set. The second one randomized the phases of Fourier components of the natural scene images, which resulted in images that had symmetric but non-Gaussian pixel value distributions, retaining the spatial correlations of the original images. A third synthetic dataset was created by independently sampling pixel values from a Gaussian distribution. In the two randomized datasets, the pixel variance was chosen to match the variance in the natural scenes.

Next, we trained our simple model on these three sets of synthetic scenes. All the trained models could perform well on their corresponding test datasets, often predicting 90% of the velocity variance (*SI Appendix*, Fig. S6). To test whether these training datasets resulted in models whose responses broke time reversal symmetry, we then presented the trained models with the edge stimulus, the stationary sawtooth stimulus, and S_{14}. When presented with edges or with the sawtooth stimulus, which possess contrast asymmetries, the models trained on the contrast reversed natural scene data broke time reversal symmetry, but in the opposite direction of the models trained on the original natural scene data (Fig. 7 *B* and *C*). For those same stimuli, the models trained with phase randomized and Gaussian scenes had responses that preserved time reversal symmetry (Fig. 7 *B* and *C*). In the case of S_{14}, which is itself contrast reversal symmetric, the contrast reversed, and natural scene trained models gave similar responses, which broke time reversal symmetry (Fig. 7*D*). Interestingly, the models trained on phase randomized and Gaussian scenes also had responses that broke time reversal symmetry, though less strongly than the other two datasets, since the time reversal symmetry metric was closer to 0 (Fig. 7*D*).

We quantified the degree of response symmetry breaking by finding the mean absolute deviation from 0 of the time reversal symmetry metric over all the models trained on each dataset (Fig. 7 *E*–*G*). This confirmed the strong symmetry breaking by models trained on natural scene statistics, and the negligible symmetry breaking by models trained on the phase randomized and Gaussian scenes, except in the case of S_{14}.

Last, we wanted to understand how model architecture influenced the degree of time reversal symmetry breaking by the trained model. We therefore trained models that had different numbers of

Downloaded from https://www.pnas.org by Nathan Wu on May 13, 2025 from IP address 178.238.172.182.

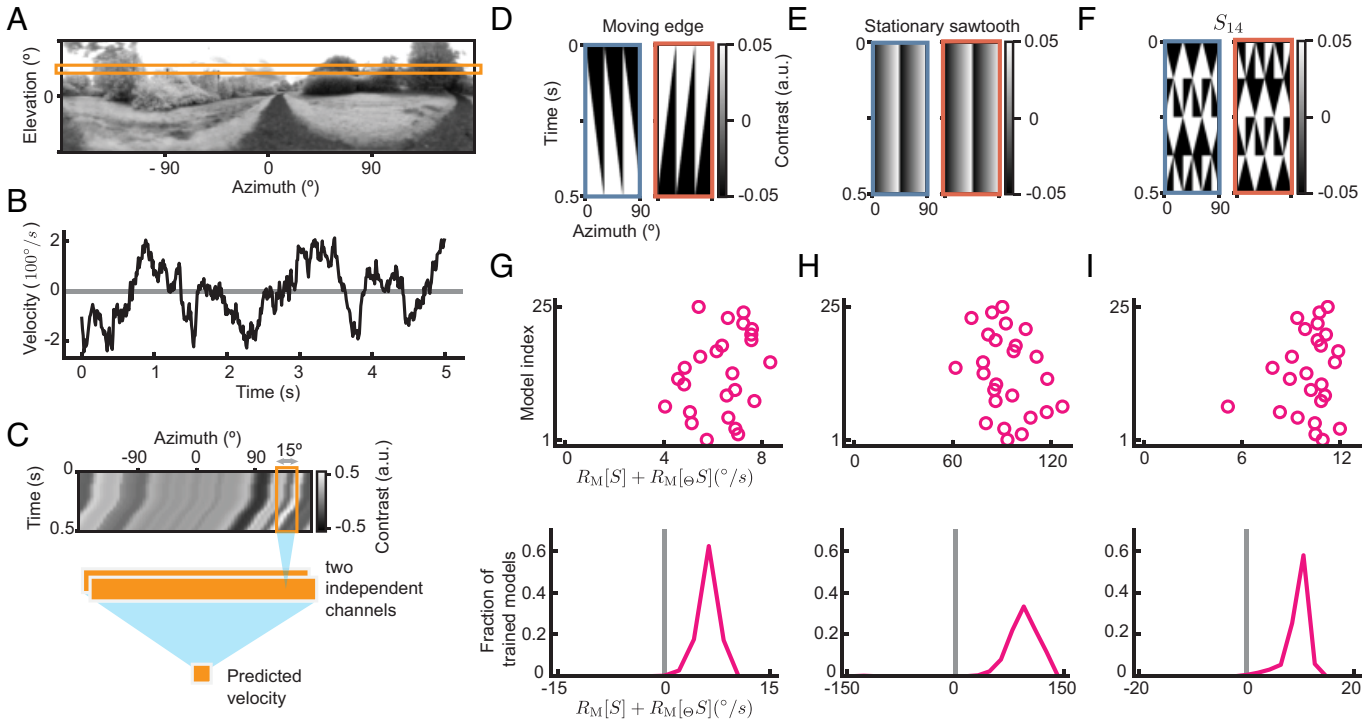

Fig. 6. Optimizing an artificial network to estimate naturalistic motion yields solutions that break time reversal symmetry. (*A*) An example panoramic natural scene image (31). The elevation spans –48° to 48° and the azimuth spans –180° to 180°. (*B*) An example velocity trajectory with autocorrelation half-decay time of 0.2 s. (*C*) Model architecture. The input to the model is motion stimuli generated by combining a horizontal slice of an image [as in (*A*)] with 0.5 s of a velocity trajectory [as in (*B*)]. The model output is the predicted velocity at the last time point of the 0.5 s velocity trajectory. There are two independent channels, and each channel spans 3 neighboring inputs in azimuth, 5° apart. (See *SI Appendix*, Methods for details.) (*D*) Moving light edge stimulus played forward (*Left*) and reversed (*Right*) in time. (*E*) Stationary contrast sawtooth stimulus played forward (*Left*) and reversed (*Right*) in time. Since the stimulus is stationary, the two versions are identical. (*F*) S_{14} played forward (*Left*) and reversed (*Right*) in time. Since the stimulus has time reversal symmetry, the two versions are identical up to a phase shift. (*G*) Time reversal symmetry metric for the model response, defined as $R_M[S] + R_M[\ominus S]$, where $R_M[S]$ is the time averaged response to the stimulus S. 25 trained models with different initializations are shown (*Top*). Distribution of $R_M[S] + R_M[\ominus S]$ for all trained models evaluated on the moving edges (*Bottom*). Only models with testing r-squared values larger than 0.8 are included. (*H*) As in (*G*), but with the model acting on the stationary sawtooth stimulus. (*I*) As in (*G*), but with the model acting on S_{14}.

channels and layers (Fig. 7*H*). We trained these models on the four datasets and measured the degree of time reversal symmetry by the mean absolute deviation from 0 of the time reversal symmetry metric of the optimized model responses. Interestingly, as we increased the number of layers, the models trained on the natural scenes and reversed contrast scenes tended to become more time reversal symmetric for the edges and sawtooth stimuli, while models trained on phase randomized and Gaussian scenes remained time reversal symmetric (Fig. 7 *I* and *J* and *SI Appendix*, Fig. S6). For S_{14}, all models but the one trained on Gaussian scenes continued to break time reversal symmetry even as their depth increased (Fig. 7*K*). Thus, the more expressive models trained on natural scenes tended to break time reversal symmetries less than shallower models for the contrast asymmetric stimuli. Meanwhile, models trained on natural and phase randomized scenes broke time reversal symmetry for S_{14}, while Gaussian scenes never resulted in trained models breaking time reversal symmetry.

To better understand these results, we also derived analytically the behavior of motion estimators that rely on different orders of correlations in the stimulus (*SI Appendix*, Appendix 2). We found that spatially mirror symmetric estimators that rely on only pairwise correlations must be time reversal symmetric, while those relying on higher-order correlations may break time reversal symmetry. Since motion estimators can use higher-order correlations, if present, to best estimate motion (14), our analytical result suggests that the non-Gaussianity of the stimulus contrast is required (but not necessarily sufficient) for trained models to break time reversal symmetry with a given stimulus, in agreement with our numerical results (Fig. 7). Our analytical results also show that when a motion estimator does break time reversal symmetry in its responses, it will exhibit this broken symmetry in response to some stimuli but not to others, with conditions that broadly agree with the experimental results shown here (Figs. 1 and 5).

Discussion

This research shows that fly motion estimation algorithms break time reversal symmetry, that is, there are stimuli for which the response to the time-reversed stimulus is not equal and opposite to the response to the original stimulus (Figs. 1, 4, and 5). This property of the response does not seem to depend strongly on the symmetry features of the stimulus (Fig. 5 and *SI Appendix*, Fig. S4). However, machine learning and analytical models for motion estimation each show that contrast asymmetries and higher-order correlations in training data can lead motion estimation algorithms to break time reversal symmetry (Figs. 6 and 7 and *SI Appendix*, Appendix 2). Interestingly, model complexity seems to suppress some types of time reversal symmetry breaking but not others (Fig. 7).

Time reversal is an understudied symmetry in neuroscience. The framework presented here focuses on the low-dimensional output of a well-studied neural computation and visual circuit. When time reversal symmetry has been used to study dynamical systems, it is typically in an unforced system, in which symmetries are studied in intrinsic dynamics of the system (37). In contrast, the symmetry breaking studied here requires the neural dynamical system to be driven by the stimulus and asks how its behavior changes under symmetry transformations of the driving stimulus. Such circuit properties are distinct from microscopic reversibility and entropy

Downloaded from https://www.pnas.org by Nathan Wu on May 13, 2025 from IP address 178.238.172.182.

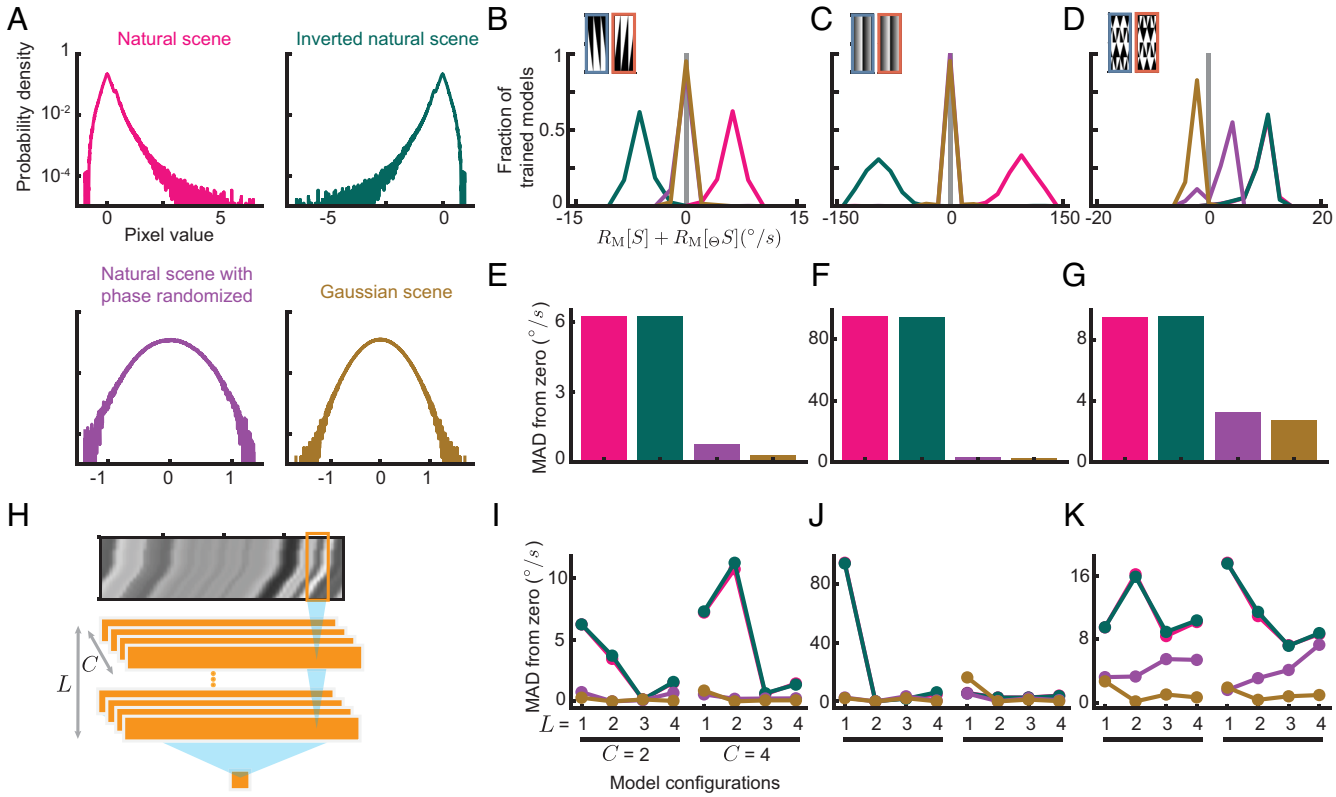

Fig. 7. Contrast distributions in training data and shallow architectures drive time reversal symmetry breaking. (*A*) Distributions of the pixel values in the four types of training data: natural scenes, contrast reversed natural scenes, natural scenes with randomized phase, and Gaussian scenes (*SI Appendix*, Methods). (*B*) Distributions of the time reversal symmetry metric, $R_M[S] + R_M[_\Theta S]$, for models trained on the four types of training data in (*A*). The models are acting on the light edge stimulus. Models are only included if they achieved an r-squared of >0.8 on their test data. (*C*) As in (*B*), but for the models acting on the stationary sawtooth stimulus. (*D*) As in (*B*), but for the models acting on S_{14}. (*E*) Mean absolute deviation (MAD) from zero of the time reversal symmetry metric $R_M[S] + R_M[_\Theta S]$ for moving edges. (*F*) As in (*E*), but for stationary sawtooth stimuli. (*G*) As in (*E*), but for S_{14}. (*H*) Model architecture was made variable so that it possessed different numbers of channels *C* and layers *L*. (*I*) MAD from zero of the time reversal symmetry metric for moving edges, but for models with different numbers of channels *C* and layers *L*. (*J*) As in (*I*), but for stationary sawtooth stimuli. (*K*) As in (*I*), but for S_{14}.

considerations studied elsewhere (16–19), instead revealing how optimization can break symmetries in surprising ways. In particular, broken isotropy in orientation detectors has been interpreted to reflect broken rotational symmetry in orientation in natural scenes (10), but here we interpret time reversal symmetry breaking as reflecting a tuning to contrast statistics, rather than broken time reversal symmetry in the system's natural inputs.

Response Time Reversal Symmetry Breaking Is Not Just Light–Dark Asymmetrical Processing. Both flies and humans process visual motion with algorithms that incorporate light–dark asymmetries (13, 38–40). The light–dark asymmetric processing has often been understood as reflecting optimization to natural scene statistics (14, 35, 36, 41). Is broken time reversal symmetry in motion responses simply another view of this contrast asymmetry in motion processing? The phenomena are related, but time reversal symmetry breaking is a broader category than the light–dark processing differences. Two lines of evidence point to a definitive distinction between the phenomena. First, the stimuli S_{14} and S_4 are each contrast reversal symmetric but both result in responses that strongly break time reversal symmetry (Fig. 5). These two examples demonstrate that time reversal symmetry breaking can occur even when all contrasts are balanced. Second, a large number of stimuli did not yield symmetrical responses under simultaneous contrast and time reversal (Fig. 5). This double transformation of the stimulus reverses time and changes all edge types from light to dark and vice versa. The time reversal transforms light edges into dark ones, but then the contrast reversal transforms them back to light ones. Thus, responses that do not exactly invert under contrast-time reversal must also result from mechanisms that are distinct from mere differences in responses to light and dark moving edges. In sum, motion estimators with light–dark asymmetric responses must break time reversal symmetry, but time reversal symmetry breaking does not imply light–dark asymmetric responses. Thus, there is a broad set of stimuli that can reveal broken time reversal symmetry in responses, even when there is no light–dark asymmetry in the response (Figs. 5 and 7).

Mixing Asymmetries in Shallow Networks. In interpreting machine learning models, we often expect symmetries in the training data to be reflected in the model. For instance, if training data for an orientation detector were isotropically distributed, we would expect an isotropic model, detecting all orientations equally. In fact, when that rotational symmetry is broken in a trained model, it is interpreted as reflecting the same broken symmetry in the stimulus (10). Interestingly, in the case we have studied here, time reversal symmetry in responses was not broken in our trained models by a broken time reversal symmetry in the training data — by construction, our training stimuli were time reversal symmetric (Fig. 6). Instead, asymmetries and non-Gaussianity in the stimulus contrast distribution led to time reversal symmetry breaking. This mixing of contrast statistics with time reversal is clear in our analytical derivation (*SI Appendix*, Appendix 2).

Optimization and Response Symmetry Breaking. Comparisons with optimized systems have proven useful in understanding the structure of motion estimating circuits and algorithms (20).

Downloaded from https://www.pnas.org by Nathan Wu on May 13, 2025 from IP address 178.238.172.182.

A Bayes optimal motion estimator will be sensitive to higher-order correlations in the inputs over time and space (14), and our analytical result suggests that this sensitivity can cause a motion estimator to break time reversal symmetry (*SI Appendix*, Appendix 2). Our artificial neural networks use threshold linear rectifiers (Figs. 6 and 7), which gives them access to both the second-order correlations in canonical models and to higher-order ones (35). Our results show that optimizing shallow neural networks to estimate velocity with natural scene inputs leads to time reversal symmetry breaking (Figs. 6 and 7), suggesting that optimization to natural scenes could explain the time reversal symmetry breaking in the fly. Deeper, more expressive networks tended to reduce time-reversal symmetry breaking associated with contrast asymmetries (Fig. 7). However, they did not reduce the response time reversal symmetry breaking of a stimulus that was light–dark symmetric. The deeper networks may be better able to extract the latent variable of velocity without considering the nuisance structure of the scene itself, but the specific symmetries retained or broken depend on the stimuli examined.

The Trained Artificial Neural Networks Do Not Reproduce Fly Percepts. We investigated how neural network architecture and training impact their time reversal symmetry to stimuli. Although the optimized networks taught us about the conditions that lead to breaking time reversal symmetry in responses, they produced responses that could or could not match the direction of the fly's responses, depending on the stimulus parameters (*SI Appendix*, Fig. S5). Prior work has shown that task optimization can recover features of the fly's motion processing, especially when connectomic constraints are incorporated (34, 42). However, the tests here may depend on more subtle differences in processing than the comparisons made in prior work. The differences between artificial networks and the fly behavior could arise because our neural networks are missing response properties that constrain the fly's responses: Processing gain changes with luminance (43), temporal and spatial contrast adaptation (44, 45), and synaptic nonlinearities in motion detectors (33, 46–48). It seems a priori unlikely that a relatively narrow, shallow neural network using threshold-linear activation functions but trained on naturalistic data would produce net responses to specific visual stimuli similar to the full biological network's behavioral output.

Similar Phenomena Across Phyla. There are many structural (9), circuit (49), and computational (50, 51) parallels between flies and mammals in visual and motion processing. The artificial neural network studies here suggest that processing that breaks time reversal symmetry could arise naturally from an optimization process, even as networks become deeper. It will therefore be interesting to examine patterns in how visual percepts break time reversal symmetry across phyla. The similar responses of flies and humans to peripheral drift illusions (1, 22), shows that time reversal symmetry is broken in motion estimation in humans. Interestingly, one form of negative triple correlation stimulus breaks time reversal symmetry in humans (13, 38), but not in flies (13). Thus, measurements of time reversal symmetry breaking percepts across species could help compare different motion estimators.

Overall, this study has shown that biological motion estimators can break time reversal symmetry under a variety of conditions. In simulations, we showed that this broken symmetry can reflect constraints on the algorithm and its tuning to the input contrast distributions. Time reversal symmetry has been largely neglected in understanding sensory processing, but investigating when it is preserved or broken can help uncover the structure of sensory computations and how they are tuned to their inputs.

Summary Methods

Drosophila behavioral data were collected by tethering flies over an air-suspended ball, presenting visual stimuli on a panoramic screen (21), and recording the ball's turning to measure the fly's intended behavior. Stimuli were presented using custom code written in Psychtoolbox (52–54) running on MATLAB (Natick, MA) and the turning response was summarized for each fly by averaging its turning over the stimulus presentation period. See *SI Appendix* for more details on the behavioral data acquisition and for details on constructing edge-tile stimuli.

Artificial neural networks were built and trained using Python and Pytorch (55). Images from a natural scene database (31) were used to create natural scene motion data in which the images were translated with stochastic velocities correlated in time (34). Inverted and phase-randomized natural scenes were obtained by transformations of the original natural scenes. The Gaussian scenes were generated by sampling the contrasts from a Gaussian distribution. A population of trained networks with different initializations were presented with stimuli to test for time reversal symmetry breaking in their responses. See *SI Appendix* for more details on the computational model architecture, training, and testing.

Data, Materials, and Software Availability. Behavioral data have been deposited in DANDI (https://doi.org/10.48324/dandi.001063/0.250125.0601) (56).

ACKNOWLEDGMENTS. We gratefully acknowledge helpful conversations with the Clark Lab, J. Demb, T. Emonet, J. Fitzgerald, C. Lynn, and J. Zavatone-Veth. This research was supported by NIH R01 EY026555 and NS121773.

1. M. Agrochao, R. Tanaka, E. Salazar-Gatzimas, D. A. Clark, Mechanism for analogous illusory motion perception in flies and humans. *Proc. Natl. Acad. Sci.* **117**, 23044–23053 (2020).
2. A. Borst, M. Egelhaaf, Principles of visual motion detection. *Trends Neurosci.* **12**, 297–306 (1989).
3. E. Adelson, J. Bergen, Spatiotemporal energy models for the perception of motion. *JOSA A* **2**, 284–299 (1985).
4. B. Hassenstein, W. Reichardt, Systemtheoretische analyse der zeit-, reihenfolgen-und vorzeichenauswertung bei der bewegungsperzeption des rüsselkäfers chlorophanus. *Zeits. Naturforsch.* **11**, 513–524 (1956).
5. M. Potters, W. Bialek, Statistical mechanics and visual signal processing. *J. Physique* **4**, 1755–1775 (1994).
6. B. D. Lucas, T. Kanade, "An iterative image registration technique with an application to stereo vision" in *IJCAI'81: 7th International Joint Conference on Artificial Intelligence*, P. J. Hayes, Ed. (Morgan Kaufmann Publishers Inc., San Francisco, CA, 1981), pp. 674–679.
7. E. Noether, Invariante variationsprobleme. *Nachr. Gesellsch. d Wiss. zu Göttingen, Math-Phys Klasse* **1**, 235–257 (1918).
8. D. J. Gross, The role of symmetry in fundamental physics. *Proc. Natl. Acad. Sci. USA* **93**, 14256–14259 (1996).
9. J. R. Sanes, S. L. Zipursky, Design principles of insect and vertebrate visual systems. *Neuron* **66**, 15 (2010).
10. A. R. Girshick, M. S. Landy, E. P. Simoncelli, Cardinal rules: Visual orientation perception reflects knowledge of environmental statistics. *Nat. Neurosci.* **14**, 926–932 (2011).
11. X. Ge *et al.*, Retinal waves prime visual motion detection by simulating future optic flow. *Science* **373**, eabd0830 (2021).
12. C. P. Ratliff, B. G. Borghuis, Y.-H. Kao, P. Sterling, V. Balasubramanian, Retina is structured to process an excess of darkness in natural scenes. *Proc. Natl. Acad. Sci. USA* **107**, 17368–17373 (2010).
13. D. A. Clark *et al.*, Flies and humans share a motion estimation strategy that exploits natural scene statistics. *Nat. Neurosci.* **17**, 296–303 (2014).
14. J. E. Fitzgerald, A. Y. Katsov, T. R. Clandinin, M. J. Schnitzer, Symmetries in stimulus statistics shape the form of visual motion estimators. *Proc. Natl. Acad. Sci. USA* **108**, 12909–12914 (2011).
15. M. M. Bronstein, J. Bruna, T. Cohen, P. Veličković, Geometric deep learning: Grids, groups, graphs, geodesics, and gauges. arXiv [Preprint] (2021). https://doi.org/10.48550/arXiv.2104.13478 (Accessed 1 December 2023).
16. C. W. Lynn, C. M. Holmes, W. Bialek, D. J. Schwab, Decomposing the local arrow of time in interacting systems. *Phys. Rev. Let.* **129**, 118101 (2022).
17. C. W. Lynn, E. J. Cornblath, L. Papadopoulos, M. A. Bertolero, D. S. Bassett, Broken detailed balance and entropy production in the human brain. *Proc. Natl. Acad. Sci. USA* **118**, e2109889118 (2021).
18. Y. S. Perl *et al.*, Nonequilibrium brain dynamics as a signature of consciousness. *Phys. Rev. E* **104**, 014411 (2021).

Downloaded from https://www.pnas.org by Nathan Wu on May 13, 2025 from IP address 178.238.172.182.

19. G. Deco *et al.*, The arrow of time of brain signals in cognition: Potential intriguing role of parts of the default mode network. *Network Neurosci.* **7**, 966–998 (2023).
20. D. A. Clark, J. E. Fitzgerald, Optimization in visual motion estimation. *Ann. Rev. Vis. Sci.* **10**, 23–46 (2024).
21. M. S. Creamer, O. Mano, R. Tanaka, D. A. Clark, A flexible geometry for panoramic visual and optogenetic stimulation during behavior and physiology. *J. Neurosci. Methods* **323**, 48–55 (2019).
22. A. Fraser, K. J. Wilcox, Perception of illusory movement. *Nature* **281**, 565–566 (1979).
23. C. Agrillo, S. Gori, M. J. Beran, Do rhesus monkeys (Macaca mulatta) perceive illusory motion? *Anim. cognit.* **18**, 895–910 (2015).
24. R. Bååth, T. Seno, A. Kitaoka, Cats and illusory motion. *Psychology* **5**, 1131–1134 (2014).
25. S. Gori, C. Agrillo, M. Dadda, A. Bisazza, Do fish perceive illusory motion? *Sci. Rep.* **4**, 6443 (2014).
26. A. Kitaoka, Phenomenal characteristics of the peripheral drift illusion. *Vision* **15**, 261–262 (2003).
27. D. A. Clark, L. Bursztyn, M. A. Horowitz, M. J. Schnitzer, T. R. Clandinin, Defining the computational structure of the motion detector in *Drosophila*. *Neuron* **70**, 1165–1177 (2011).
28. M. S. Maisak *et al.*, A directional tuning map of *Drosophila* elementary motion detectors. *Nature* **500**, 212–216 (2013).
29. A. Leonhardt *et al.*, Asymmetry of *Drosophila* ON and OFF motion detectors enhances real-world velocity estimation. *Nat. Neurosci.* **19**, 706–715 (2016).
30. M. Silies *et al.*, Modular use of peripheral input channels tunes motion-detecting circuitry. *Neuron* **79**, 111–127 (2013).
31. H. G. Meyer, A. Schwegmann, J. P. Lindemann, M. Egelhaaf, *Panoramic High Dynamic Range Images in Diverse Environments*. (Bielefeld University, 2014).
32. K. Shinomiya *et al.*, Comparisons between the ON-and OFF-edge motion pathways in the *Drosophila* brain. *eLife* **8**, e40025 (2019).
33. J. A. Zavatone-Veth, B. A. Badwan, D. A. Clark, A minimal synaptic model for direction selective neurons in *Drosophila*. *J. Vis.* **20**, 2–2 (2020).
34. O. Mano, M. S. Creamer, B. A. Badwan, D. A. Clark, Predicting individual neuron responses with anatomically constrained task optimization. *Curr. Biol.* **31**, 4062–4075 (2021).
35. J. E. Fitzgerald, D. A. Clark, Nonlinear circuits for naturalistic visual motion estimation. *eLife* **24**, e09123 (2015).
36. J. Chen, H. B. Mandel, J. E. Fitzgerald, D. A. Clark, Asymmetric ON-OFF processing of visual motion cancels variability induced by the structure of natural scenes. *eLife* **8**, e47579 (2019).
37. J. S. Lamb, J. A. Roberts, Time-reversal symmetry in dynamical systems: A survey. *Physica D: Nonlinear Phenomena* **112**, 1–39 (1998).
38. Q. Hu, J. D. Victor, A set of high-order spatiotemporal stimuli that elicit motion and reverse-phi percepts. *J. Vis.* **10**, 1–16 (2010).
39. G. Mather, B. Moulden, A. O'Halloran, Polarity specific adaptation to motion in the human visual system. *Vision Res.* **31**, 1013–1019 (1991).
40. B. Moulden, H. Begg, Some tests of the Marr-Ullman model of movement detection. *Perception* **15**, 139 (1986).
41. E. I. Nitzany, J. D. Victor, The statistics of local motion signals in naturalistic movies. *J. Vis.* **14**, 10 (2014).
42. J. K. Lappalainen *et al.*, Connectome-constrained networks predict neural activity across the fly visual system. *Nature* **634**, 1132–1140 (2024).
43. M. D. Ketkar, S. Shao, J. Gjorgjieva, M. Silies, Multifaceted luminance gain control beyond photoreceptors in *Drosophila*. *Curr. Biol.* **33**, 2632–2645.e2636 (2023).
44. M. S. Drews *et al.*, Dynamic signal compression for robust motion vision in flies. *Curr. Biol.* **30**, 209–221 2020).
45. C. A. Matulis, J. Chen, A. Gonzalez-Suarez, R. Behnia, D. A. Clark, Heterogeneous temporal contrast adaptation in *Drosophila* direction-selective circuits. *Curr. Biol.* **30**, 222–236 (2020).
46. E. Gruntman, S. Romani, M. B. Reiser, Simple integration of fast excitation and offset, delayed inhibition computes directional selectivity in *Drosophila*. *Nat. Neurosci.* **21**, 250–257 (2018).
47. B. A. Badwan, M. S. Creamer, J. A. Zavatone-Veth, D. A. Clark, Dynamic nonlinearities enable direction opponency in *Drosophila* elementary motion detectors. *Nat. Neurosci.* **22**, 1318–1326 (2019).
48. L. N. Groschner, J. G. Malis, B. Zuidinga, A. Borst, A biophysical account of multiplication by a single neuron. *Nature* **603**, 119–123 (2022).
49. A. Borst, M. Helmstaedter, Common circuit design in fly and mammalian motion vision. *Nat. Neurosci.* **18**, 1067–1076 (2015).
50. D. A. Clark, J. B. Demb, Parallel computations in insect and mammalian visual motion processing. *Curr. Biol.* **26**, R1062–R1072 (2016).
51. J. Chen *et al.*, Direct comparison reveals algorithmic similarities in fly and mouse visual motion detection. *iScience* **26**, 107928 (2023).
52. D. G. Pelli, The VideoToolbox software for visual psychophysics: Transforming numbers into movies. *Spatial vision* **10**, 437–442 (1997).
53. M. Kleiner *et al.*, What's new in Psychtoolbox-3. *Perception* **36**, 1 (2007).
54. D. H. Brainard, The psychophysics toolbox. *Spatial vision* **10**, 433–436 (1997).
55. A. Paszke *et al.*, Pytorch: An imperative style, high-performance deep learning library. *Adv. Neural Inform Proc. Sys.* **32**, 8026–8037 (2019).
56. N. Wu, Broken time reversal symmetry in motion detection. DANDI Archive. https://doi.org/10.48324/dandi.001063/0.250125.0601. Deposited 24 January 2025.

Downloaded from https://www.pnas.org by Nathan Wu on May 13, 2025 from IP address 178.238.172.182.